

pubs.acs.org/journal/ascecg Research Article

Surfactant-Assisted Exfoliation of Tantalum Diboride (TaB₂) for Electrochemical CO₂ Reduction

Published as part of ACS Sustainable Chemistry & Engineering special issue "Celebrating the 25th Anniversary of the Chemical Research Society of India".

Anshul Rasyotra, Anupma Thakur, Shreya Shukla, Raviraj Mandalia, Raghavan Ranganathan, and Kabeer Jasuja*



Cite This: ACS Sustainable Chem. Eng. 2025, 13, 2312–2323



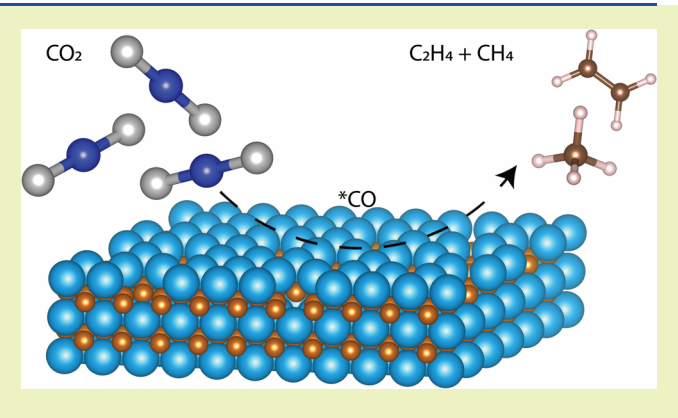
ACCESS

III Metrics & More

Article Recommendations

Supporting Information

ABSTRACT: Recent years have witnessed a renewed interest in utilizing AlB₂-type metal borides for applications traditionally not envisaged for this family of ionic layered materials. This is due to a native synergy between the metal atoms and boron honeycomb planes that imparts them versatile physicochemical properties. This prospect is further augmented by their feasibility to be nanoscaled into quasi-two-dimensional (2D) forms–XBenes, as demonstrated by several recent studies. In this work, we show that such a nanoscale can also be extended to tantalum diboride (TaB₂), a member of this family that has largely remained uncharted. We found that TaB₂ can be exfoliated into few-layer-thick nanosheets (mean thickness of 4.5 nm) by using surfactant chemistry. The resultant nanosheets were found to retain their structural integrity to a large extent. We utilized the readily accessible Ta–B sites



offered by these nanosheets to catalyze the electrochemical reduction of aqueous CO_2 . Moreover, we found that these TaB_2 nanosheets facilitate the production of ethylene as the main carbon product, with faradaic efficiency reaching 75% at -0.85 V vs RHE. We obtain additional insights using DFT studies, which show how the interaction of CO_2 with Ta and B atoms results in favorable CO_2 adsorption for ethylene production.

KEYWORDS: 2D materials, XBenes, borophene, tantalum diboride, ethylene, CO2 reduction

■ INTRODUCTION

Massive fossil fuel consumption and increasing CO₂ concentration in the atmosphere have emphasized the importance of utilizing CO₂ to synthesize value-added products renewably.^{1,2} In this regard, electrochemical CO₂ reduction reaction (CO₂RR) shines as one of the most prominent approaches, owing to the ambient reaction conditions and its implications in mitigating high carbon emissions.^{3,4}

The most common products obtained through the CO_2RR are the low-value C1 products. The formation of these C1 products is more prevalent because of the chemical inertness of the CO_2 molecule and sluggish kinetics of the C-C coupling reaction, which is vital for the formation of C_{2+} species. Among the C_{2+} products, ethylene is the most desirable due to its large market consumption among all reaction products. While several materials have been reported in the literature for catalyzing the electrochemical reduction of CO_2 , few facilitate the synthesis of ethylene. Further, the majority of such catalysts that lead to ethylene formation are Cu-based. 8,10,11

There has been a growing interest in finding catalysts alternative to Cu for enabling the reduction of CO_2 to ethylene, as evidenced in the recent reports on boron-doped nanodiamonds and graphene quantum dots. Some theoretical studies have also reported the use of the mechanism of ethylene production for a rational design of alternative catalysts. For example, Li *et al.* have suggested that the two-dimensional (100) plane enables a selective formation of C_{2+} species by virtue of a double bridge ensemble site on the surface. $\mathrm{^{11,15}}$

In this connection, AlB₂-type metal diborides present a rich prospect for catalyzing CO₂RR on account of their structural arrangement that comprises alternate planes of boron and

Received: August 13, 2024 Revised: January 15, 2025 Accepted: January 16, 2025

Published: January 27, 2025





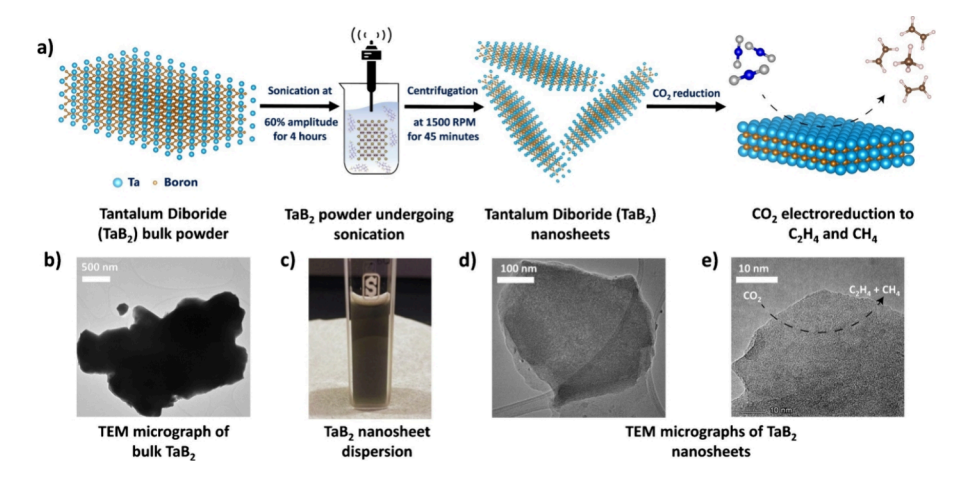


Figure 1. (a) Synthesis scheme to exfoliate TaB_2 nanosheets in sodium cholate solution and their utilization for the electrochemical synthesis of ethylene and methane, (b) TEM image of bulk TaB_2 (c) TaB_2 nanosheets dispersed in sodium cholate solution, and (d, e) TEM images of TaB_2 nanosheets.

metal atoms, with the (100) plane being the most dominant. The last few years have witnessed several metal diborides being utilized as catalysts for various electrochemical reactions. Yuan et al. recently showed that these metal diborides have extremely low limiting potential for CO_2 reduction, with OsB_2 having the lowest potential of -0.4 eV for CH_4 production.²¹ The ability to exfoliate these metal diborides into their quasi-2D forms further augments these prospects. We recently coined the name XBenes for these quasi-2D materials derived from MB2 phases. It is pertinent to note that these XBenes differ from materials derived from MAB phases known as MBenes. Owing to the presence of vacancies and dynamic surface reordering, the XBenes have higher chemical and thermal durability for electrochemical activities than conventional catalysts. 17,22-26 This is exemplified in the reports by Joshi et al. and Rasyotra et al., wherein they utilized TiB2 nanosheets for hydrogen production and nitrogen reduction, respectively. 25,27,2

This feasibility of delaminating AlB₂-type metal diborides (such as MgB₂ and TiB₂) presents a foundation for developing quasi-2D forms in other members of this family. In the context of the CO₂ reduction reaction, TaB₂, a member of this metal diboride family that has largely remained uncharted, is particularly intriguing (Figure S1, SI). The metal atom tantalum (Ta) present in TaB₂ has a unique electronic structure, which makes it a potential candidate for various electrocatalytic applications, including electrochemical CO₂ reduction. Researchers have also shown that Ta atoms can induce C–C coupling that could potentially initiate the synthesis of C₂₊ products. This motivated us to extend the exfoliation approaches to TaB₂ and investigate the candidacy of the resultant quasi-2D forms for electrochemical CO₂ reduction.

In this work, we present three seminal developments. First, we show that TaB_2 can be exfoliated into few-layer-thick nanosheets using ultrasonication in the presence of sodium cholate. The resultant nanosheets exhibit a mean thickness of \sim 4.5 nm and retain their native crystallinity. Second, the TaB_2 nanosheets are found to exhibit superlative catalytic activity for CO_2 reduction and deliver an ethylene faradaic efficiency of 75% (Figure 1a). Third, the DFT studies show how charge transfer among the CO_2 molecules and Ta-B atoms results in CO_2 activation to produce ethylene. Also, the high FE

obtained for ethylene is attributed to the presence of Ta-B active sites that favor C-C coupling. To the best of our knowledge, this work presents the first report on the synthesis of TaB_2 nanosheets and their utilization as electrocatalysts for CO_2 reduction. This constitutes a significant addition to the growing literature on non-Cu-based catalysts for ethylene production and catalytic properties of metal diborides.

MATERIALS AND METHODS

Synthesis of TaB₂ Nanosheets. TaB₂ nanosheets were synthesized by adopting the experimental procedure from our previous study.²⁵ This method is based on surfactant-assisted exfoliation of bulk metal diborides, in which sodium cholate is used as the surfactant. Briefly, 1 g of bulk TaB2 crystals (Sigma-Aldrich, 99% pure, size <10 μ m) were initially added to 20 mL of deionized (DI) water (Millipore Ultrapure Type II, ionic conductivity = 18.2 MΩ·cm (25 °C)). The mixture was probe sonicated for 20 min at 25% amplitude using a QSonica Q500 probe sonicator, followed by centrifugation at 10,000 rpm. The cleaned TaB2 crystals (sediment) were recovered and added to 100 mL of 2 g/L sodium cholate solution. This mixture was probe sonicated for 4 h at 60% amplitude in 6 s ON/2 s OFF cycles. The temperature was kept constant using an ice bath. The black suspension obtained after sonication was centrifuged at 1500 rpm for 45 min, and the top ~3/4 volume was collected and utilized for further characterization and electrode preparation.

Structural Characterization. The transmission electron microscopy (TEM) micrographs were acquired using ThermoFisher FEI, Titan Themis (60-300 keV), operated at 300 keV. The sample for TEM was prepared by preparing 1 mg/mL of TaB2 nanosheet dispersion in DI water and diluting it 100 times. Ten µL of this dispersion was taken and drop cast on the TEM grids (Ted Pella lacey carbon grids, 300 mesh, 3 mm diameter). The HRTEM images were processed using GATAN digital micrograph software, and various FFT, inverse FFT, and line profiles were obtained. The same dispersion was also utilized to prepare samples for AFM. The AFM images were captured using a Bruker NanoWizard Sense AFM instrument operated in tapping mode using a Sb-doped silica cantilever (spring constant = 3 N/m and frequency = 75 kHz). For deposition, 20 μ L of the dispersion was taken and spin-coated (3000 rpm, 30 s) on freshly cleaved mica substrates (PELCO Ted Pella, 9.9 mm diameter). The spin-coated material was then left to dry under ambient conditions.

Chemical Characterization. UV-vis spectroscopic studies of the nanosheets were performed on a Shimadzu UV-1800 spectrophotometer in the 200–1100 nm range by using quartz cuvettes having a path length of 1 cm. Dispersions of different concentrations were

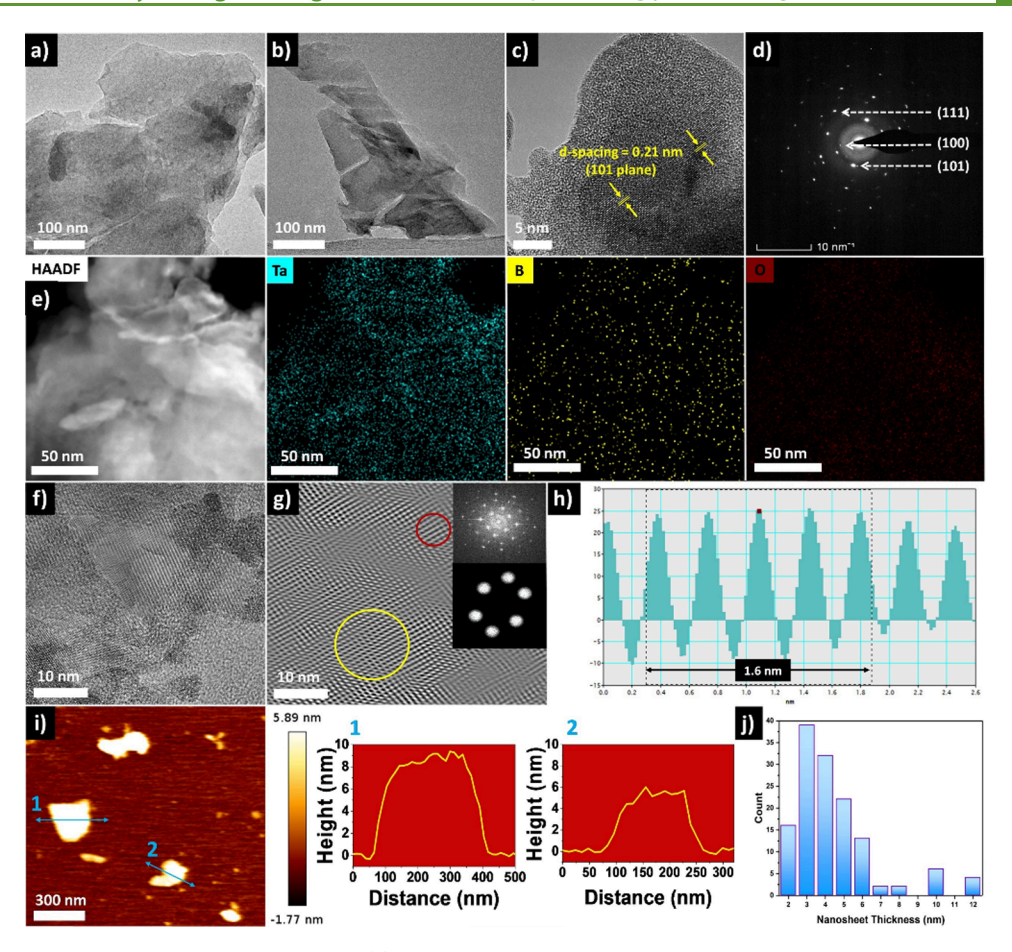


Figure 2. (a, b) TEM micrographs of TaB₂ nanosheets. (c) HR-TEM micrograph of a nanosheet indicating a *d*-spacing of 0.21 nm. (d) SAED pattern showing the polycrystalline nature of the exfoliated nanosheet. (e) high-angle annular dark field (HAADF) combined with scanning transmission electron microscopy-electron dispersive X-ray (STEM-EDX) mapping of a single TaB₂ nanosheet. (f) HR-TEM micrograph of a nanosheet utilized for generating a (g) simulated micrograph. The yellow circle in the micrograph indicates a pristine region, and the red circle indicates a small area where defects can be observed. The micrograph inset shows the simulated SAED pattern of the nanosheet and mask applied to generate the image. (h) Line profile was generated using the simulated micrograph to calculate the *d*-spacing. (i) AFM image, topographical analysis, and representative height profiles of two nanosheets. (j) Histogram representing the thickness of the nanosheets corresponding to the exfoliated nanosheets.

prepared using serial dilutions from the stock dispersion at a 0.2 mg/mL concentration. The XRD spectra of bulk TaB_2 and TaB_2 nanosheets were recorded using a Bruker D8 instrument equipped with $Cu-K\alpha$ (1.54 Å) radiation. The XPS studies of the bulk TaB_2 and TaB_2 nanosheets were performed on a Thermofisher Scientific Nexsa Base with monochromatic $Al-K\alpha$ X-ray with an energy of 1486.6 eV.

Electrochemical Characterization. The electrochemical measurements were performed in an H-cell under ambient conditions using the Metrohm AutoLab M204 instrument (NOVA 2.1 software). Three-electrode systems were used in the measurements: platinum wire electrode as the counter electrode, Ag/AgCl electrode (3 M KCl) as the reference electrode, and nanosheets deposited on indium tin oxide (ITO) as the working electrode. The cyclic voltammetry (CV) studies were conducted at scan rates of 10–100 mV/s. The prepared electrodes' electrochemical impedance spectra (EIS) were obtained by sweeping the frequencies from 10⁵ Hz to 0.1 Hz under a 10 mV AC perturbation signal. CV and EIS were used to map the performance of as-fabricated electrodes in a 5 mM ferri/ferro redox aqueous solution containing 0.1 M KCl. The areal capacitance (C) from the CV responses at different scan rates was calculated using the following equation:

$$C = \frac{\int I(E) dE}{2\nu \Delta E} \tag{1}$$

Here, I(E) is the current at the electrode potential E, ν is the scan rate, and ΔE is the electrode potential window in which the scan is performed. The explanation for the equation of areal capacitance has been included in the Supporting Information. The linear sweep voltammetry (LSV) studies were performed with a scan rate of 1 mV/s, and EIS studies were conducted by sweeping the frequencies from 10^{5} to 0.1 Hz under a 10 mV AC perturbation signal. The electrode potentials after iR compensation were rescaled to the reversible hydrogen electrode (RHE) using the following equation:

$$E_{\text{RHE}} = E_{\text{Ag/AgCl}} + 0.199 + 0.059^{*} \text{pH}$$
 (2)

For electrode preparation, 250 μ L of a 2 mg mL⁻¹ nanosheet dispersion was spin-coated on the conductive side of the ITO (spin coat area of 0.5 cm⁻²), resulting in a catalyst loading of 1 mg cm⁻². Aqueous 0.1 M KHCO₃ was used as an electrolyte. Before the reaction, the electrolyte was saturated with N₂ for 5 min, followed by the addition of CO₂ gas (99.999%) for 30 min. CO₂ was continuously bubbled into the electrolyte at a rate of 20 sccm during the experiment. The electrolyte was stirred using a Teflon-coated magnetic stir bar at 500 rpm to enhance the mass flow of CO₂ to the working electrode. The stability of the TaB₂ nanosheets was evaluated with chronoamperometry tests at a constant current potential applied for a duration of 20,000 s. The length of all chronoamperometry experiments was fixed at 1 h before the gas products were collected for analysis. Gas-phase products were

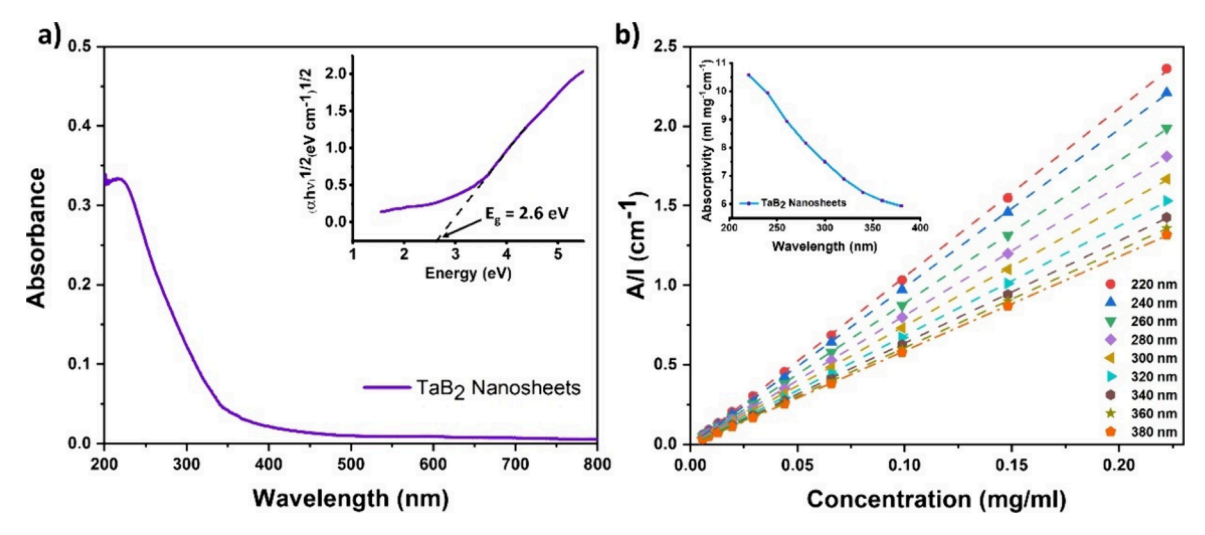


Figure 3. (a) UV—vis spectra of the exfoliated TaB₂ nanosheets in the dispersion, showing absorbance in the ultraviolet region with a peak centered at 220 nm. The inset of the graph shows the Tauc plot generated from the absorption spectra indicating an indirect band gap of 2.6 eV for these nanosheets. (b) Absorptivity values calculated at different wavelengths. The inset of the graph shows the dependence of absorptivity with the wavelength.

quantified using a gas chromatograph (GC) equipped with a flame ionization detector (FID). The faradaic efficiency (FE) of the gaseous product was calculated using

$$FE = \frac{n_e \times x \times F \times \text{flowrate} \times P}{R \times T \times I}$$
(3)

where n_e is the number of moles of electrons required to obtain 1 molecule of product, x is the concentration of gaseous product formed in ppm, P is ambient pressure (101325 Pa), T is ambient temperature, F is the Faraday constant (96485 C mol⁻¹), R is gas constant (8.314 J K⁻¹ mol⁻¹), and I is average current density during sampling time.

DFT Simulations. The spin-polarized calculations presented here were performed in the Vienna Ab initio Simulation Package (VASP) based on the GGA Perdew–Burke–Ernzerhof exchange-correlation functional $^{37-39}$ and is similar to our previous work. 20,25 The DFT-D3 method within the Grimme scheme included the van der Waals interactions. 40 The energy cutoff for plane wave expansion was set as 400 eV. The convergence criteria for geometric optimization were set as 10^{-9} eV for total energy and 10^{-4} eV Å $^{-1}$ for maximum force. The Brillouin zone was sampled with an automatic 3 \times 3 \times 1 grid of k-points. The optimized TaB2 unit cell is used to generate a 3 \times 3 \times 3 slab structure of TaB2 with a 20 Å vacuum in the [0 0 1] direction. The top two layers were unconstrained and free to interact with the adsorbents, whereas the bottom 5 layers were held fixed to their bulk configuration.

The optimized unit cell of TaB_2 and the replicated one $(3 \times 3 \times 3 \text{ slabs})$ are shown in Figure S9, SI. Adsorption energies were studied for pristine TaB_2 of Ta (001)-exposed surface for CO_2 adsorption (Figure S10, SI). CO_2 fixation represents the initial step in CO_2 reduction. Therefore, given its highly electropositive nature, the Ta surface is selected for exposure, facilitating strong CO_2 adsorption on the TaB_2 layer. Average adsorption energies were calculated using the equation:

$$\Delta E_{*x} = E_t - E_x - E_* \text{ and } \Delta E_{\text{avg}-x} = \Delta E_{*x}/n \tag{4}$$

where $\Delta E_{*_{\rm x}}$ is the adsorption energy, $E_{\rm t}$ is the total energy of the catalyst with adsorbed species, $E_{\rm x}$ is the energy of the adsorbed species, E_* is the energy of the catalyst surface, and n is the number of interacting atoms contributing to the active site, here, the top one Ta layer of TaB₂.

RESULTS AND DISCUSSION

For synthesizing the TaB₂ nanosheets, we adopted a surfactant-based exfoliation approach recently developed by us.²⁵ The

bulk TaB₂ powder (Figure 1b) was initially cleaned to remove unwanted impurities (see methods for more details). The cleaned TaB2 powder was probe-sonicated in sodium cholate solution and centrifuged to remove the unexfoliated or partially exfoliated particles to obtain a homogeneous dispersion (Figure 1c). This surfactant-based exfoliation approach was chosen because it helps preserve the long-range crystallinity and minimizes the functionalization of nanosheets, which in turn would facilitate enhanced access to the planes of metal and boron atoms. Although organic solvents could also be utilized to obtain pristine nanosheets,8 these are expensive, toxic, and difficult to handle, making their dispersions difficult to process. Also, organic solvents themselves transform into optically active 2D nanostructures during ultrasonicationassisted exfoliation. We chose sodium cholate as the surfactant because it is a biosurfactant with no persistent, bioaccumulative, or toxic components. Furthermore, this approach would allow the dispersion of TaB₂ nanosheets in water, aiding in the easy preparation of working electrodes for electrochemical applications.

We acquired transmission electron microscopy (TEM) micrographs of the dispersed structures and observed sheetlike nanostructures with lateral dimensions in the range of 100-500 nm (Figures 1d,e and 2a,b). The nanosheets observed under TEM were extremely transparent compared to the bulk TaB2 crystals, indicating that a successful exfoliation has been achieved. Figure 2c shows a highresolution transmission electron microscopy (HRTEM) micrograph of a TaB2 nanosheet having lattice fringes with a dspacing of 0.21 nm. We also collected selected area electron diffraction (SAED) patterns of these nanosheets to determine the degree of crystallinity (Figure 2d). SAED patterns indicated that these nanosheets exhibit ordered spots that correspond to the (100), (101), and (111) planes, suggesting that the crystallinity was retained after exfoliation. We also captured a high-angle annular dark-field (HAADF) image of a representative nanosheet and combined it with scanning transmission electron microscopy-electron dispersive X-ray (STEM-EDX) mapping to obtain information about the chemical composition. Figure 2e presents the mapped

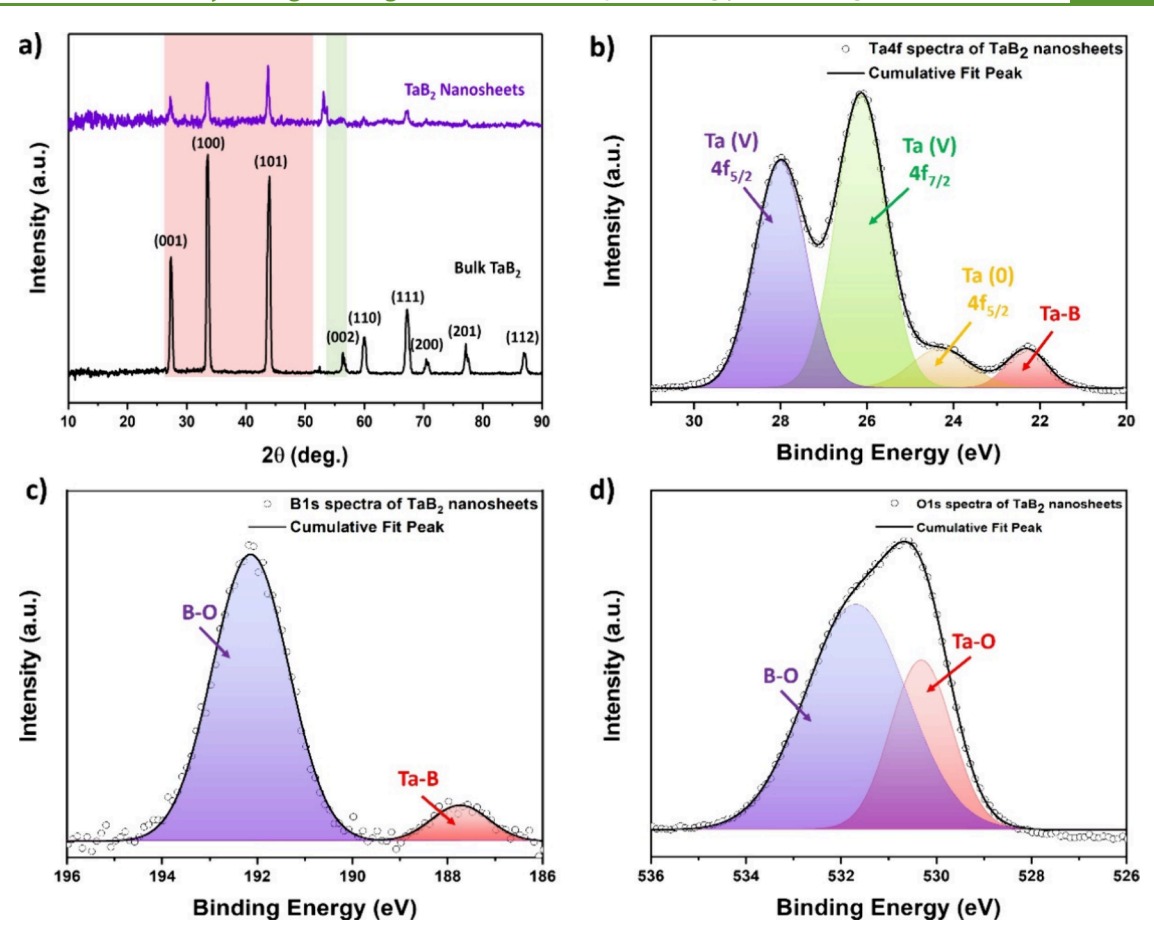


Figure 4. (a) XRD spectra of Bulk TaB_2 and TaB_2 nanosheets showing peaks at similar positions and matching with PDF-03-065-7834 in the ICDD. These positions indicate the retained structural integrity of the nanosheets. The pink box highlights the three primary planes of TaB_2 retained after exfoliation, and the green box indicates the Ta_2O_5 species formed as a result of exfoliation. (b) Ta 4f spectra, (c) B 1s spectra, and (d) O 1s spectra of the nanosheets showing peaks corresponding to Ta—B bonding and some oxy-functionalization. These spectra are acquired using XPS.

elements from a selected region of the nanosheet. The nanosheet showed strong and concurrent signals of tantalum and boron and a weak signal of oxygen, indicating that while some oxy-functional groups are sparsely scattered on the nanosheet, the chemical integrity of the nanosheets was retained to a considerable extent. The presence of boron was affirmed by using X-ray photoelectron spectroscopy (XPS) and inductively coupled plasma atomic emission spectroscopy (ICP-AES) analysis, as discussed later. We also collected an HRTEM micrograph of a representative nanosheet and generated a simulated micrograph using fast Fourier transform (FFT) and inverse FFT (Figure 2f,g). The micrograph and the generated SAED pattern indicate an ordered honeycomb arrangement, confirming the crystalline nature of the nanosheets.²⁴ Using the line profile generated from the micrograph, we calculated the d-spacing to be 0.21 nm, which corresponds to the (101) plane of TaB₂. This is also supplemented by XRD results as described ahead.

To confirm the quasi-2D nature of the nanosheets, we performed an atomic force microscopy (AFM) analysis. Figure 2i (1 and 2) presents the area scan and the height profiles of two representative nanosheets, indicating thickness values of ~ 9 and ~ 6 nm, respectively. We measured the thickness of 136 nanosheets and obtained a mean thickness of 4.5 nm, indicating that these nanosheets are a few layers thick (Figure 2j).

We obtained insights into the optical properties of these TaB₂ nanosheets using UV-vis spectroscopy. The nanosheets exhibited absorption over a wide range of visible light-NIR regions with a peak in the UV region (Figure 3a). The peak centered at 220 nm can be attributed to the $n \to \pi^*$ transitions that stem from the presence of oxy-functional groups. 22,41,42 We have explained this aspect in detail in the XRD section ahead. The nanosheets had an indirect band gap of 2.6 eV, calculated by using the Tauc plot. This value is lesser when compared with the other exfoliated metal diborides reported in the literature $(MgB_2 - 4.49 \text{ eV} \text{ and } TiB_2 - 3.5 \text{ eV})^{.25,43,44}$ The lower band gap value for these TaB2 nanosheets makes them suitable candidates for optical and photonic applications. We also obtained absorption profiles of the nanosheet dispersion at different predetermined concentrations to generate concentration calibration curves and utilized these to calculate the absorptivity values (Figures S2, S3, and SI). The absorptivity values decreased with the increasing wavelength, achieving a maximum value of 10.58 mg⁻¹ cm⁻¹ mL at 220 nm (Figure 3b). This value was higher compared with other metal diboride nanosheets derived from MgB2 and TiB2, however, with a magnitude less than that of the other 2D materials.44 This difference suggests that these nanosheets are more transparent than other 2D materials such as graphene and MoS2, and can likely be used in applications that require transparent coatings.

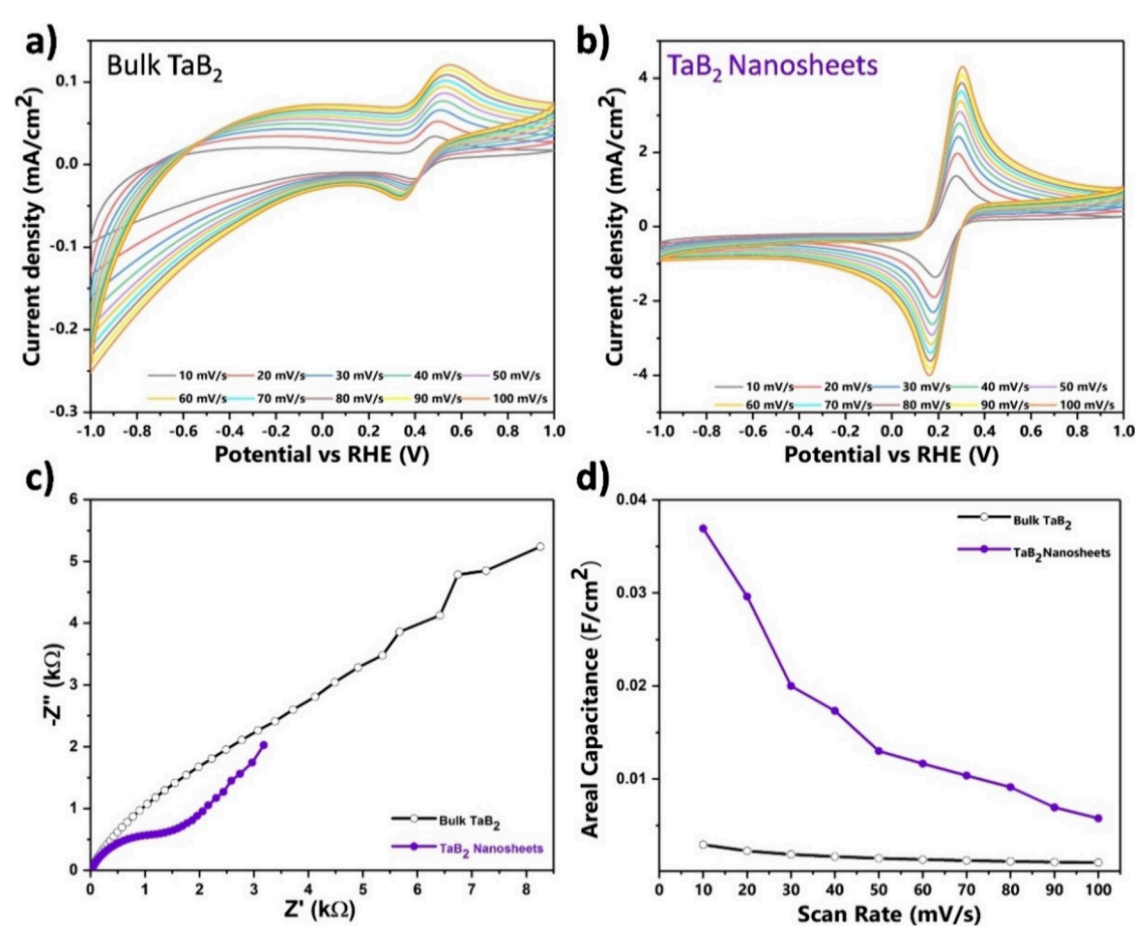


Figure 5. Electrochemical characterization of TaB₂ nanosheets. Cyclic voltammograms of (a) bulk TaB₂ and (b) TaB₂ nanosheets in 5 mM ferri/ ferro redox aqueous solution containing 0.1 M KCl with a scan rate of 10–100 mV/s. (c) Nyquist plot showing lower charge transfer resistance for TaB₂ nanosheets and (d) change in areal capacitance with increasing scan rates.

To obtain insights into the structure of these nanosheets, we performed X-ray diffraction (XRD) studies (Figure 4a). The XRD spectra of TaB₂ nanosheets indicated no shift in the peak positions compared with the peaks observed in the bulk TaB₂. However, we observed two differences in the spectra—(a) peak broadening and (b) decrease in intensity. This difference is expected due to the reduced crystallite size and a decrease in the number of layers in TaB₂ crystal after exfoliation.^{24,45} We also observed an enhancement in the peak intensity for nanosheets at 53° that corresponds to the formation of Ta₂O₅, indicating some degree of oxy-functionalization. This little increase in intensity is possibly due to an exposure of the nonbonded Ta atoms to the surroundings after the exfoliation. The concurrent presence of peaks corresponding to the two primary planes of TaB2, along with the formation of Ta2O5, indicates that functionalization was limited to the surface of these nanosheets.

We obtained further insights into the chemical interface of these nanosheets using X-ray photoelectron spectroscopy (XPS) analysis. Figure 4b presents the Ta 4f spectra of the TaB₂ nanosheets exhibiting four peaks. The first two peaks at 22.2 eV (4f_{7/2}) and 24.3 eV (4f_{5/2}) correspond to the Ta–B bonding. The other two peaks centered at 26.1 eV (4f_{7/2}) and 28 eV (4f_{5/2}) correspond to the oxidized tantalum, representing mild oxy-functionalization. We observed a slight increase in the binding energies of the peaks in Ta 4f spectra of TaB₂ nanosheets compared with bulk TaB₂ (Figure S4a, SI).

This increase is possibly due to the ultrasonication that causes the removal of some atoms, resulting in stronger binding among the remaining atoms. The B 1s spectra of the TaB_2 nanosheets show two peaks centered at 187.7 and 192.14 eV (Figure 4c). The first peak is the characteristic peak of metal diborides, and the latter peak corresponds to boron oxides (B_2O_3). Similarly, the two peaks in the O 1s spectra centered at 530.3 and 531.7 eV correspond to Ta-O and B-O bonding (Figure 4d). We performed ICP-AES analysis to corroborate the presence of Ta and B and found that the nanosheets exhibit a Ta:B stoichiometry of 0.91:2.

We further explored the electrochemical properties of these nanosheets, encouraged by the previous results of different members of the metal diboride family. 20,24 The electrochemical properties of the TaB2 nanosheets were initially evaluated using a standard ferri/ferro electrolyte. The working electrode was prepared by depositing TaB2 nanosheets/bulk TaB₂ powder onto an ITO slide. The reference electrode was Ag/AgCl, while the counter electrode was a platinum wire. Before measurements, the standard ferri/ferro electrolyte was saturated with N2 gas to eliminate dissolved oxygen. Initially, we obtained the cyclic voltammetry (CV) characteristics of the bulk TaB₂ and TaB₂ nanosheets at different scan rates (Figure 5a,b). The redox peaks for bulk TaB₂ were observed at 0.325 V (reduction) and 0.55 V (oxidation), whereas the corresponding redox peaks for TaB2 nanosheets were observed at 0.15 V (reduction) and 0.3 V (oxidation) at a scan rate of 10 mV/s.

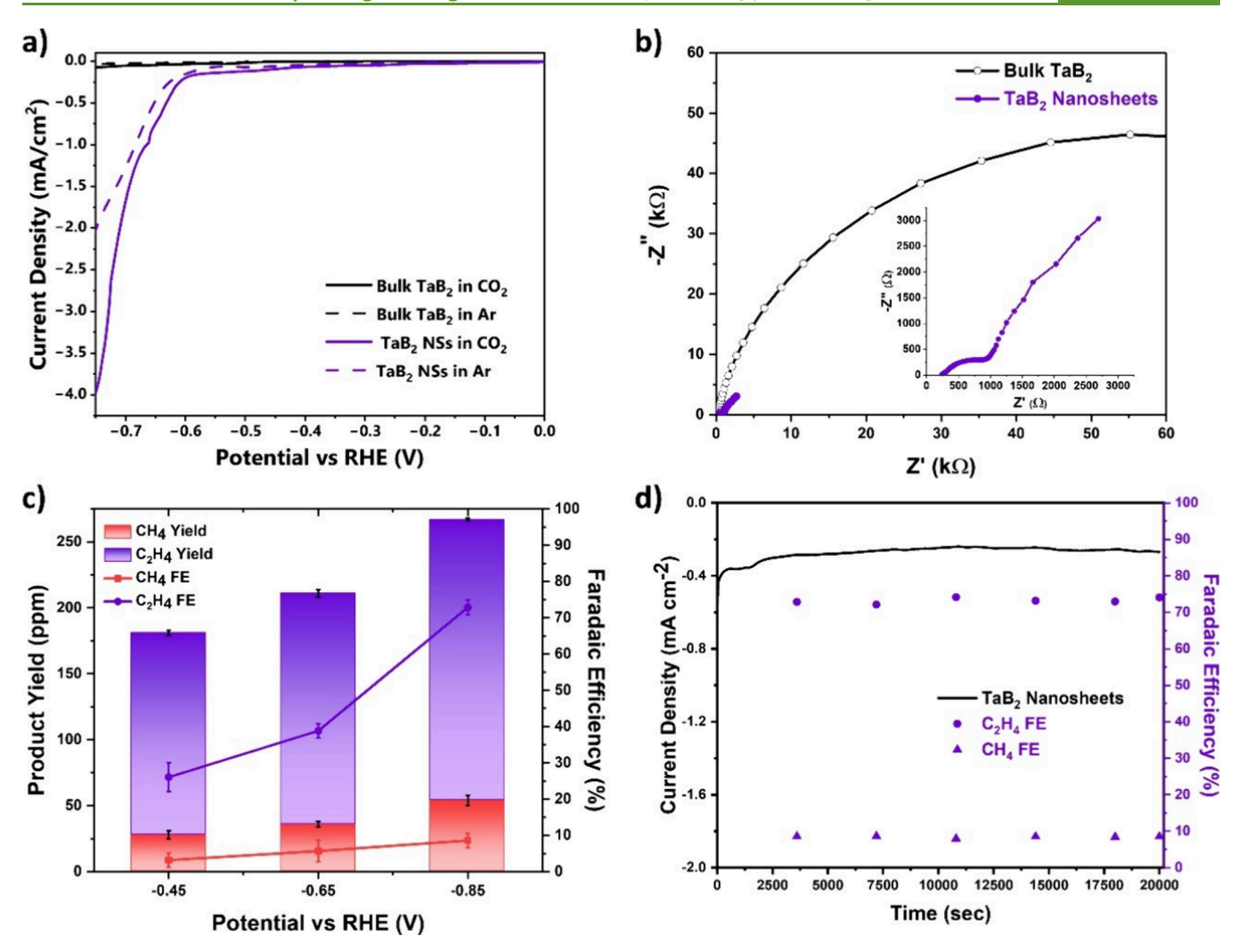


Figure 6. Electrochemical carbon dioxide reduction reaction using TaB_2 nanosheets. (a) Linear sweep voltammograms of bulk TaB_2 and TaB_2 nanosheets in CO_2 - and Ar-purged 0.1 M KHCO₃ with a scan rate of 1 mV/s. (b) Nyquist plot showing lower charge transfer resistance for TaB_2 nanosheets as compared with bulk TaB_2 in CO_2 -purged 0.1 M KHCO₃, (c) FE and product yield measured at different potentials with error bars representing the standard deviation of measurements based on three independent samples, and (d) current density and FE were measured at a constant potential of -0.85 V versus RHE for TaB_2 nanosheets during the stability study for 20,000 s. The circle and triangle symbols represent the FE obtained for C_2H_4 and CH_4 respectively.

We found an 80-fold increment in the anodic and cathodic current for the nanosheets compared with bulk TaB_2 . Such a significant increase in the current densities can be attributed to the enhanced accessibility of surface atoms upon exfoliation, which results in more electrochemically active sites.

To obtain more insights into the electrochemical nature of the nanosheets, we measured the electrochemical impedance spectra (EIS) in ferri/ferro electrolytes. These measurements were carried out by sweeping the frequencies from 10⁵ to 0.1 Hz (Figure 5c). Randle's equivalent circuit was used to measure the charge transfer resistance (R_{ct}) (Figure S5, SI). We observed a reduction in the $R_{\rm ct}$ values for TaB₂ nanosheets compared with those of bulk TaB2. The Rct value decreased from 5.52 $k\Omega$ for bulk TaB_2 to 1.11 $k\Omega$ for the TaB_2 nanosheets, indicating an enhancement in the electron transfer kinetics. This decrease in R_{ct} was expected since TaB₂ nanosheets would be more conducive to charge transfer due to the presence of more active sites. Additionally, the areal capacitance (C) of TaB₂ nanosheets was 40 mF/cm² at a scan rate of 10 mV/s (Figure 5d), which was substantially higher than that of bulk TaB_2 (~1.5 mF/cm²). This increase in areal

capacitance can similarly be attributed to the higher surface area-to-volume ratio, facilitating more active sites for charge storage.²⁴

These promising results from the electrochemical characterization of TaB_2 nanosheets motivated us to further test their candidacy as a catalyst for CO_2 reduction. This hypothesis was based on two reasons. First, Ta atoms exhibit an inherent ability to activate the CO_2 molecules. This happens due to the interaction of the 5d orbital of Ta with the CO_2 molecule, which causes changes in their local electronic structure. ^{33,35} Second, the presence of electron-deficient boron in the structure imparts properties of Lewis basicity in the transition metal atoms, and this synergy, in turn, is known to facilitate CO_2 reduction. ^{47,48} The presence of these active sites on the basal plane makes these nanosheets highly accessible for facilitating CO_2 reduction. ^{21,49}

We performed linear sweep voltammetry (LSV) studies to obtain preliminary insights into the electrochemical CO₂ reduction activity of these TaB₂ nanosheets. Since the ferri/ferro electrolyte does not provide a suitable environment for the CO₂ reduction reaction, the electrocatalytic performance

was evaluated in CO2- and Ar-purged 0.1 M KHCO3 electrolytes in an H-cell (refer to methods for additional details). We observed that the TaB2 nanosheets exhibit a much higher current density in the CO₂-saturated electrolyte compared with that of the Ar-saturated electrolyte (Figure 6a). This indicates that these TaB₂ nanosheets were indeed catalytically active for the CO₂RR. We also conducted similar LSV studies for the bulk TaB₂. The current density for TaB₂ nanosheets in a CO₂-saturated electrolyte was much higher compared with bulk TaB2. This increase can be attributed to the higher density of active sites due to edges and the active basal plane within the nanosheets. 16,18,20 Also, nanosheets have the advantage of increased surface area-to-volume ratio that can promote efficient mass transport of reactants and products to and from the catalyst surface, thereby enhancing the overall reaction kinetics. 11,16 Although the catalytic activity of bulk TaB2 was several folds lower than TaB2 nanosheets, a comparison of curves obtained from Ar-saturated electrolyte and CO₂-saturated electrolyte indicates that TaB₂ is catalytically active for CO₂RR in its bulk form as well. These results demonstrate the merit of revisiting metal diborides for their catalytic properties.

To explore the reaction dynamics of the TaB2 nanosheets during CO₂ reduction, we performed EIS studies by sweeping the frequencies from 1×10^5 to 0.1 Hz. Figure 6b indicates the EIS spectra for bulk TaB2 and TaB2 nanosheets-their corresponding Randle's equivalent circuits have been shown in Figure S6, SI. The charge transfer resistance (R_{ct}) of TaB₂ nanosheets (275 Ω) was found to be several folds lower than that of bulk TaB_2 (103 k Ω). The low value of charge transfer resistance demonstrates the enhanced activity of TaB2 nanosheets, thereby promoting CO₂RR performance.²⁴ These results also explain the higher current density of the TaB2 nanosheets observed in LSV curves. To gain insights into the density of electrochemically active sites, we calculated electrochemical surface area (ECSA) using double-layer capacitance (C_{dl}) values obtained from CV measurements in the nonfaradaic region.^{24,50} The ECSA was calculated by dividing the $C_{\rm dl}$ value by specific capacitance ($C_{\rm s}$), where a $C_{\rm s}$ value of 40 $\mu \rm F~cm^{-2}$ was utilized. As shown in Figure S7, SI, TaB₂ nanosheets exhibit a high ECSA of 0.73 cm² which is much higher compared with that of the bulk TiB₂.

To understand the fate of CO₂ upon reduction, we analyzed the synthesized products obtained at three different potentials using gas chromatography (GC, see methods for details). We found that at all these potentials, ethylene (C_2H_4) was forming as the main product, accompanied by a relatively small amount of methane (CH₄), as shown in Figures 6c and S8, SI. As mentioned by Liu et al., C2+ product formation is invariably accompanied by a small amount of low-carbon products due to the multistep electron transfer.⁵² The presence of ethylene in the synthesized product validates our hypothesis that C-C bond coupling can indeed be realized by using the Ta-B sites. This is the first experimental report on utilizing TaB₂ nanosheets as an electrocatalyst for C2+ product synthesis. We also calculated the faradaic efficiency (FE) at different potentials (see the methods for more details). We achieved an FE of 30% for C_2H_4 and 5% for CH_4 at -0.45 V vs RHE. These values increased to 75% (C₂H₄) and 10% (CH₄) at -0.85 V vs RHE (Figure 6c). This increase in the FE at a more negative potential of -0.85 V vs RHE suggests that the Ta-B sites in the TaB₂ nanosheets were more favorable for the formation of C₂H₄ compared with CH₄. It is plausible that at

-0.85 V vs RHE, the dimerization of crucial intermediate *CO is favored, resulting in higher FE for C_2H_4 . 52,53 This is also supported by the minor increase in the FE of CH_4 as explained in the DFT studies ahead. Above -0.85 V vs RHE, H_2 production primarily becomes dominant, which would result in decreasing FEs for both C_2H_4 and CH_4 . 53 The FE reported here for C_2H_4 is at par with the traditionally used Cu-based catalysts and higher than the non-Cu catalysts reported in the literature (Table S1, SI).

This superlative activity of TaB2 nanosheets was sustained over a long duration, as supported by the chronoamperometric measurements. These measurements were performed at a constant current potential of -0.85 V vs RHE for a duration of 20,000 s (Figure 6d). The current density was found to be stable at ~ 0.3 mA/cm², suggesting the durability of these TaB₂ nanosheets as a CO2 reduction electrocatalyst. We also measured the FE of C2H4 and CH4 at different intervals during the CO₂RR and found the nanosheets to exhibit an FE of 75% ± 5%. These stable values of FE over an extended duration of 20,000 s suggest minimal degradation under operating conditions, which is crucial for practical applications. As explained above, the CO₂RR ability of these nanosheets is attributed to the charge transfer between the Ta-B sites and the CO₂ molecules. We also acknowledge that surfactants can lower the surface tension of the material, thereby resulting in fast mass transfer, quick gas release, and hence, an increase in the electrochemical performance of oxygen evolution reaction (OER). However, since CO₂ reduction and C₂₊ product formation are known to be limited by the C-C coupling reaction, it is the active sites in the nanosheets that would play the central role in governing the overall efficiency and yield of the products obtained.

The higher efficiency achieved by these TaB2 nanosheets and their stability for CO2 reduction also makes these nanosheets environmentally sustainable in terms of waste generation. The synthesis route of sodium cholate solutionbased exfoliation, which is environmentally safer than the traditionally used surfactants, further adds to the sustainable nature of these nanosheets.⁵⁴ Moreover, TaB₂ nanosheets are heterogeneous catalysts that can be easily handled and separated. Such features could easily affect the overall economic costs of utilizing these catalysts and result in a more efficient process, thereby making a step toward sustainable systems.⁵⁵ The presented TaB₂ nanosheets exhibit a high selectivity toward electrocatalytic CO2 conversion into C₂ products. This contributes to mitigating climate change by utilizing CO2 as a feedstock rather than allowing it to accumulate as a greenhouse gas. The catalytic process facilitated by TaB2 nanosheets operates under milder conditions, requiring less energy input compared to conventional methods. This reduction in energy consumption is a critical factor in enhancing the overall sustainability of the CO₂RR process. 56,57 While copper-based catalysts have a strong track record for selective ethylene production from electrocatalytic CO2 reduction, TaB2 nanosheets present a more sustainable and potentially cost-effective alternative. The enhanced stability, environmentally safer synthesis, and practical advantages of TaB2 nanosheets make them a promising candidate for sustainable CO₂ reduction processes. Additionally, the high surface area and active sites, coupled with improved reaction kinetics and high FE, position TaB₂ nanosheets as a viable alternative to conventional copper-based catalysts. These benefits highlight TaB2 nanosheets as a viable

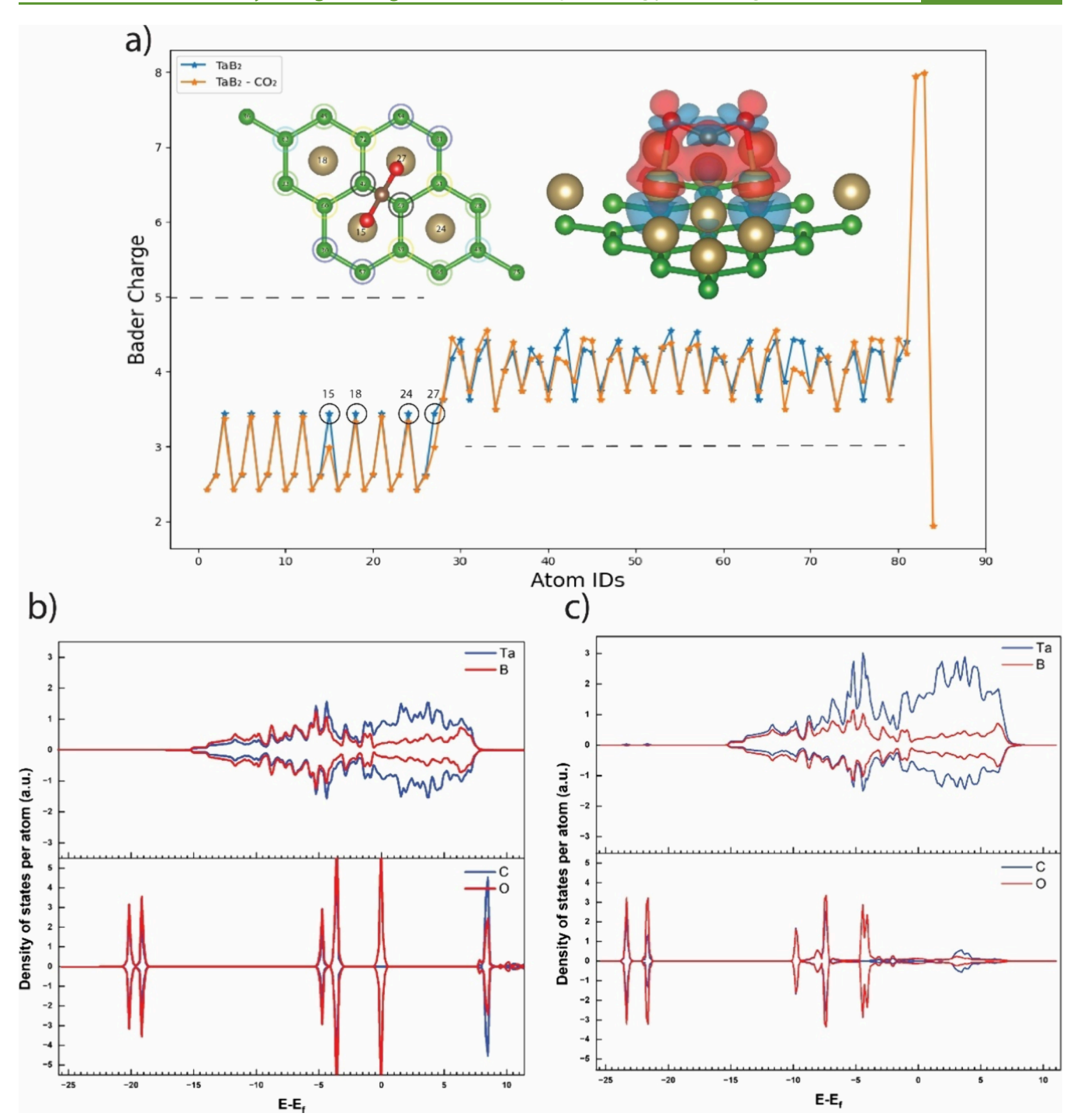


Figure 7. (a) Bader charge analysis of the Ta (light brown) and B (green) atoms in TaB_2 before and after CO_2 (C dark brown and O-red) adsorption. The Ta atoms (atom IDs 15 and 27) and the B atoms (atom IDs 42 and 69) that have the maximum charge transfer are highlighted. The other B atoms in the two hexagonal rings that have a reduced charge transfer are also highlighted. The inset in panel (a) shows the charge density difference plot for the TaB_2 nanosheet with adsorbed CO_2 molecule using the optimized charge density of pristine TaB_2 , CO_2 , and TaB_2 – CO_2 . After the adsorption of CO_2 , the red area (positive) represents the accumulation of charge, and the blue area (negative) represents the depletion of charge. (b) and (c) PDOS plots for pristine TaB_2 nanosheet and free CO_2 molecule (b) and the nanosheet and adsorbed CO_2 molecule (c) showing the redistribution of hybridized orbital energies after adsorption.

and environmentally friendly quasi-2D nanostructured catalyst option, particularly in applications where overall sustainability and long-term economic viability are critical considerations. 58,59

To gain further insights into the role played by TaB_2 nanosheets in the CO_2 reduction reaction, we performed density functional theory (DFT) calculations. Figure 7 shows

the results from the electron transfer process during the adsorption of CO_2 on a pristine Ta-exposed nanosheet, which is the crucial step for CO_2 activation. As shown in Figure 7a, the Bader charge analysis shows that the most important sites that participate in CO_2 adsorption are the 2 Ta atoms directly below the CO_2 (along the short diagonal), apart from 10 B atoms that are closest to CO_2 (Figure 7a, left inset). The Bader

charge analysis reveals that after the adsorption, there is a charge transfer from Ta and B atoms to CO₂. The calculation setup considers Ta, B, O, and C with 5, 3, 6, and 4 electrons, respectively; the corresponding Bader charges are shown in Table S2, SI.

Additionally, two Ta atoms along the long diagonal also contribute partially toward adsorption. Interestingly, the B sublattice directly below the Ta surface seems to play a vital role in adsorption, unlike the recent finding of N2 adsorption on the TiB2 surface, where the role played by B atoms was insignificant.²⁵ We observed that two hexagonal boron rings just below CO₂ predominantly have a depletion of charge density, resulting in a small increase of charge density on the peripheral B atoms (Figure 7a, inset). Thus, the adsorption of CO₂ is facilitated by charge transfer from both Ta and B to CO₂. Moreover, the partial density of states (PDOS) analysis sheds light on the nature of charge transfer (Figure 7b). We found that the 2p orbitals of C and O atoms actively participate in the hybridization with Ta and B orbitals with a shift of the hybridized orbitals of CO2 to the left, indicating stable bonds. The Projected Density of States (PDOS) for pristine and CO₂-adsorbed TaB₂ are shown in Figure S11, SI. We observe that the Ta 5d, C-2p, and O-2p actively participate (undergo hybridization) in the adsorption. Notably, close to the Fermi level, the occupied 2p orbitals of C and O have a strong interaction with Ta 5d states, there is a significant redistribution of the states, and the peaks are shifted to the left. The current work serves as a starting point for a more detailed characterization of the role played by defects such as vacancies as well as the adsorption energies and mechanisms of the reduction pathways consisting of intermediates using DFT studies.

CONCLUSIONS

In summary, we synthesized TaB₂ nanosheets using an environmentally sustainable approach, adding a new member to the XBenes family. We utilized the Ta-B sites offered by these TaB2 nanosheets to produce ethylene via electrochemical CO₂ reduction. We achieved a faradaic efficiency of 75% for the formation of ethylene owing to the enhanced access to Ta atoms incorporated on boron honeycombs. The DFT studies show that significant charge transfer occurs during the adsorption of CO₂ on pristine TaB₂ nanosheets, with the Ta and B atoms in the immediate vicinity of adsorbed CO₂ lending the maximum charge transfer to CO₂. To our knowledge, this study presents the first report on the utilization of TaB2 nanosheets as an electrocatalyst to reduce CO2 and obtain C₂₊ products. The absorption coefficient and band gap reported here for the TaB2 nanosheets also make them suitable candidates for photonic and surface coatings applications. This work showcases the merit of exploring new members of the metal diboride family and the diversity they offer for various catalytic applications.

ASSOCIATED CONTENT

Supporting Information

The Supporting Information is available free of charge at https://pubs.acs.org/doi/10.1021/acssuschemeng.4c06710.

Microscopic and structural characterization of TaB_2 nanosheets, their electrochemical characterization and other catalytic data, additional DFT data sets (PDF)

AUTHOR INFORMATION

Corresponding Author

Kabeer Jasuja — Department of Chemical Engineering, Indian Institute of Technology Gandhinagar, Gandhinagar, Gujarat 382355, India; ⊚ orcid.org/0000-0002-4332-0712; Email: kabeer@iitgn.ac.in

Authors

Anshul Rasyotra — Department of Chemical Engineering, Indian Institute of Technology Gandhinagar, Gandhinagar, Gujarat 382355, India; orcid.org/0000-0001-7294-4420

Anupma Thakur – Department of Chemical Engineering, Indian Institute of Technology Gandhinagar, Gandhinagar, Gujarat 382355, India

Shreya Shukla — Department of Materials Engineering, Indian Institute of Technology Gandhinagar, Gandhinagar, Gujarat 382355, India

Raviraj Mandalia – Department of Materials Engineering, Indian Institute of Technology Gandhinagar, Gandhinagar, Gujarat 382355, India

Raghavan Ranganathan — Department of Materials Engineering, Indian Institute of Technology Gandhinagar, Gandhinagar, Gujarat 382355, India; orcid.org/0000-0003-1015-791X

Complete contact information is available at: https://pubs.acs.org/10.1021/acssuschemeng.4c06710

Author Contributions

§A.R. and A.T. contributed equally.

Notes

The authors declare no competing financial interest.

ACKNOWLEDGMENTS

We want to acknowledge the central instrumentation facility of IIT Gandhinagar for providing various instrumental facilities. We also thank AMRC-IIT Mandi for the XPS analysis. K.J. acknowledges the funding support from the seed grant IITGN, Core Research Grant (No. EMR/2017/000730) by the Department of Science and Technology India, Core Research Grant (No. CRG/2023/008191) by SERB India, and STARS Research Grant (No. MoE-STARS/STARS-2/2023-1024) by Ministry of Education, India. K.J. also acknowledges the funding provided by Dr. Dinesh O Shah Chair Fellowship. R.R. acknowledges support for computational facilities at the Param Ananta supercomputing facility (IIT Gandhinagar). A.T. acknowledges funding through the IITGN Early Career Fellowship (Grant MIS/IITGN/R&D/KJ/202122/028). The authors also acknowledge the Department of Scientific and Industrial Research (DSIR) for Common Research & Technological Development Hub (CRTDH) (Grant DSIR/ CRTDH/NM/IIT-Gn/2016) facility use. The authors also thank the chemical engineering office staff, Mr. Supresh, Mr. Suvakanta, Mr. Rajib and Mr. Rohit, for their constant assistance in our day-to-day work.

REFERENCES

- (1) Solomon, S.; Plattner, G. K.; Knutti, R.; Friedlingstein, P. Irreversible Climate Change Due to Carbon Dioxide Emissions. *Proc. Natl. Acad. Sci. U. S. A.* **2009**, *106* (6), 1704–1709.
- (2) De Luna, P.; Hahn, C.; Higgins, D.; Jaffer, S. A.; Jaramillo, T. F.; Sargent, E. H. What Would It Take for Renewably Powered Electrosynthesis to Displace Petrochemical Processes? *Science* **2019**, 364 (6438), No. eaav3506.

- (3) Jiang, K.; Sandberg, R. B.; Akey, A. J.; Liu, X.; Bell, D. C.; Nørskov, J. K.; Chan, K.; Wang, H. Metal Ion Cycling of Cu Foil for Selective C–C Coupling in Electrochemical CO2 Reduction. *Nat. Catal.* **2018**, *1* (2), 111–119.
- (4) Liu, C.; Colón, B. C.; Ziesack, M.; Silver, P. A.; Nocera, D. G. Water Splitting–Biosynthetic System with CO₂ Reduction Efficiencies Exceeding Photosynthesis. *Science* **2016**, 352 (6290), 1210–1213.
- (5) Todorova, T. K.; Schreiber, M. W.; Fontecave, M. Mechanistic Understanding of CO ₂ Reduction Reaction (CO2RR) Toward Multicarbon Products by Heterogeneous Copper-Based Catalysts. *ACS Catal.* **2020**, *10* (3), 1754–1768.
- (6) Schouten, K. J. P.; Kwon, Y.; van der Ham, C. J. M.; Qin, Z.; Koper, M. T. M. A New Mechanism for the Selectivity to C1 and C2 Species in the Electrochemical Reduction of Carbon Dioxide on Copper Electrodes. *Chem. Sci.* **2011**, 2 (10), 1902–1909.
- (7) Peter, S. C. Reduction of CO ₂ to Chemicals and Fuels: A Solution to Global Warming and Energy Crisis. ACS Energy Lett. **2018**, 3 (7), 1557–1561.
- (8) Qu, J.; Cao, X.; Gao, L.; Li, J.; Li, L.; Xie, Y.; Zhao, Y.; Zhang, J.; Wu, M.; Liu, H. Electrochemical Carbon Dioxide Reduction to Ethylene: From Mechanistic Understanding to Catalyst Surface Engineering. *Nanomicro Lett.* **2023**, *15*, 178.
- (9) Han, N.; Ding, P.; He, L.; Li, Y.; Li, Y. Promises of Main Group Metal—Based Nanostructured Materials for Electrochemical CO ₂ Reduction to Formate. *Adv. Energy Mater.* **2020**, *10*, No. 1902338.
- (10) Gao, S.; Jiao, X.; Sun, Z.; Zhang, W.; Sun, Y.; Wang, C.; Hu, Q.; Zu, X.; Yang, F.; Yang, S.; Liang, L.; Wu, J.; Xie, Y. Ultrathin Co $_3$ O $_4$ Layers Realizing Optimized CO $_2$ Electroreduction to Formate. *Angew. Chem., Int. Ed.* **2016**, 55 (2), 698–702.
- (11) Zhang, X.; Guo, S.-X.; Gandionco, K. A.; Bond, A. M.; Zhang, J. Electrocatalytic Carbon Dioxide Reduction: From Fundamental Principles to Catalyst Design. *Mater. Today Adv.* **2020**, *7*, No. 100074.
- (12) Liu, Y.; Zhang, Y.; Cheng, K.; Quan, X.; Fan, X.; Su, Y.; Chen, S.; Zhao, H.; Zhang, Y.; Yu, H.; Hoffmann, M. R. Selective Electrochemical Reduction of Carbon Dioxide to Ethanol on a Boron- and Nitrogen-Co-doped Nanodiamond. *Angew. Chem., Int. Ed.* **2017**, *56* (49), 15607–15611.
- (13) Wu, J.; Ma, S.; Sun, J.; Gold, J. I.; Tiwary, C.; Kim, B.; Zhu, L.; Chopra, N.; Odeh, I. N.; Vajtai, R.; Yu, A. Z.; Luo, R.; Lou, J.; Ding, G.; Kenis, P. J. A.; Ajayan, P. M. A Metal-Free Electrocatalyst for Carbon Dioxide Reduction to Multi-Carbon Hydrocarbons and Oxygenates. *Nat. Commun.* **2016**, *7* (1), 13869.
- (14) Song, Y.; Chen, W.; Zhao, C.; Li, S.; Wei, W.; Sun, Y. Metal-Free Nitrogen-Doped Mesoporous Carbon for Electroreduction of CO₂ to Ethanol. *Angew. Chem., Int. Ed.* **2017**, *56* (36), 10840–10844.
- (15) Li, H.; Li, Y.; Koper, M. T. M.; Calle-Vallejo, F. Bond-Making and Breaking between Carbon, Nitrogen, and Oxygen in Electrocatalysis. *J. Am. Chem. Soc.* **2014**, *136* (44), 15694–15701.
- (16) Thakur, A.; Rasyotra, A.; Jasuja, K. Review and Perspectives of Electrochemical Energy Conversion and Storage in Metal Diborides and XBenes. *Energy Fuels* **2023**, *37*, 18310.
- (17) Chakrabarty, S.; Thakur, A.; Rasyotra, A.; Gaykwad, B.; Jasuja, K. Quasi-Two-Dimensional Nanostructures from AlB2-Type Metal Borides: Physicochemical Insights and Emerging Trends. *J. Phys. Chem. C* **2023**, *127* (2), 852–870.
- (18) Gunda, H.; Klebanoff, L. E.; Sharma, P. A.; Varma, A. K.; Dolia, V.; Jasuja, K.; Stavila, V. Progress, Challenges, and Opportunities in the Synthesis, Characterization, and Application of Metal-Boride-Derived Two-Dimensional Nanostructures. *ACS Mater. Lett.* **2021**, 3 (5), 535–556.
- (19) Zhang, B.; Zhou, J.; Sun, Z. MBenes: Progress, Challenges and Future. J. Mater. Chem. A Mater. 2022, 10, 15865.
- (20) Rasyotra, A.; Thakur, A.; Gaykwad, B.; Mandalia, R.; Ranganathan, R.; Jasuja, K. Vacancy Rich TiB ₂ Nanosheets Promote Electrochemical Ammonia Synthesis. *ACS Appl. Mater. Interfaces* **2024**, *16*, 24473.
- (21) Yuan, H.; Li, Z.; Yang, J. Transition-Metal Diboride: A New Family of Two-Dimensional Materials Designed for Selective CO2 Electroreduction. *J. Phys. Chem. C* **2019**, *123* (26), 16294–16299.

- (22) James, A. L.; Lenka, M.; Pandey, N.; Ojha, A.; Kumar, A.; Saraswat, R.; Thareja, P.; Krishnan, V.; Jasuja, K. Processable Dispersions of Photocatalytically Active Nanosheets Derived from Titanium Diboride: Self Assembly into Hydrogels and Paper-like Macrostructures. *Nanoscale* **2020**, *12*, 17121.
- (23) Yousaf, A.; Gilliam, M. S.; Chang, S. L. Y.; Augustin, M.; Guo, Y.; Tahir, F.; Wang, M.; Schwindt, A.; Chu, X. S.; Li, D. O.; Kale, S.; Debnath, A.; Liu, Y.; Green, M. D.; Santos, E. J. G.; Green, A. A.; Wang, Q. H. Exfoliation of Quasi-Two-Dimensional Nanosheets of Metal Diborides. *J. Phys. Chem. C* 2021, 125 (12), 6787–6799.
- (24) Gaykwad, B.; Thakur, A.; Buch, A.; Jasuja, K. Large-Scale Synthesis of Electrochemically Active Titanium Diboride-Based Nanosheets by High-Energy Ball Milling. *J. Phys. Chem. C* **2023**, 127, 15887—15900.
- (25) Rasyotra, A.; Thakur, A.; Mandalia, R.; Ranganathan, R.; Jasuja, K. Nitrogen Adsorption via Charge Transfer on Vacancies Created during Surfactant Assisted Exfoliation of TiB2. *Nanoscale* **2023**, *15* (18), 8204–8216.
- (26) Jani, V.; Rasyotra, A.; Gunda, H.; Ghoroi, C.; Jasuja, K. Titanium Diboride (TiB₂) Derived Nanosheets Enhance the CO₂ Capturing Ability of Calcium Oxide (CaO). *Ceram. Int.* **2022**, 48 (21), 32380–32388.
- (27) Joshi, G.; Chakrabarty, S.; Khatua, S.; Jasuja, K. TiB2 Derived Nanosheets Co-Immobilized with Triangular Gold Nanoparticles Elicit Fast and Stable Photocatalytic Hydrogen Evolution. *Int. J. Hydrogen Energy* **2022**, *52*, 20–32.
- (28) Li, S.; Gunda, H.; Ray, K. G.; Wong, C.-S.; Xiao, P.; Friddle, R. W.; Liu, Y.-S.; Kang, S.; Dun, C.; Sugar, J. D.; Kolasinski, R. D.; Wan, L. F.; Baker, A. A.; Lee, J. R. I.; Urban, J. J.; Jasuja, K.; Allendorf, M. D.; Stavila, V.; Wood, B. C. Spontaneous Dynamical Disordering of Borophenes in MgB2 and Related Metal Borides. *Nat. Commun.* 2021, 12 (1), 6268.
- (29) Elsayed, N.; El-Rabiei, M. M.; Negem, M.; Heakal, F. E.-T. The Potential of Tantalum as an Efficient Electrocatalyst for Green Hydrogen Production. *Electrochim. Acta* **2022**, *404*, No. 139783.
- (30) Ruiz-Cornejo, J. C.; Sebastián, D.; Martínez-Huerta, M. V.; Lázaro, M. J. Tantalum-Based Electrocatalysts Prepared by a Microemulsion Method for the Oxygen Reduction and Evolution Reactions. *Electrochim. Acta* **2019**, *317*, 261–271.
- (31) Rasool, A.; Anis, I.; Dixit, M.; Maibam, A.; Hassan, A.; Krishnamurty, S.; Dar, M. A. Tantalum Based Single, Double, and Triple Atom Catalysts Supported on g-C ₂ N Monolayer for Effective Nitrogen Reduction Reaction: A Comparative DFT Investigation. *Catal. Sci. Technol.* **2022**, *12* (1), 310–319.
- (32) Matsuyama, T.; Kikkawa, S.; Kawamura, N.; Higashi, K.; Nakatani, N.; Kato, K.; Yamazoe, S. CO₂ Activation on Lindqvist-Type Polyoxotantalate: Structural Analysis by In Situ HERFD-XANES. J. Phys. Chem. C 2024, 128 (7), 2953–2958.
- (33) Sarabadani Tafreshi, S.; Panahi, S.; Fatemeh, K. S.; Taghizade, N.; Jamaati, M.; Ranjbar, M.; de Leeuw, N. H. Thermodynamic and Kinetic Study of Carbon Dioxide Hydrogenation on the Metal-Terminated Tantalum-Carbide (111) Surface: A DFT Calculation. *Catalysts* **2022**, *12* (10), 1275.
- (34) Sändig, N.; Koch, W. A Quantum Chemical View on the Mechanism of the Ta ⁺ -Mediated Coupling of Carbon Dioxide with Methane. *Organometallics* **1998**, *17* (11), 2344–2351.
- (35) Lengyel, J.; Levin, N.; Ončák, M.; Jakob, K.; Tschurl, M.; Heiz, U. Direct Coupling of Methane and Carbon Dioxide on Tantalum Cluster Cations. *Chem.–Eur. J.* **2023**, 29 (9), No. e202203259.
- (36) Dutta, N.; Bagchi, D.; Chawla, G.; Peter, S. C. A Guideline to Determine Faradaic Efficiency in Electrochemical CO ₂ Reduction. *ACS Energy Lett.* **2024**, 9 (1), 323–328.
- (37) Kresse, G.; Furthmüller, J. Efficient Iterative Schemes for Ab Initio Total-Energy Calculations Using a Plane-Wave Basis Set. *Phys. Rev. B Condens Matter Mater. Phys.* **1996**, 54 (16), 11169–11186.
- (38) Kresse, G.; Furthmüller, J. Efficiency of Ab-Initio Total Energy Calculations for Metals and Semiconductors Using a Plane-Wave Basis Set. *Comput. Mater. Sci.* **1996**, *6* (1), 15–50.

- (39) Kresse, G.; Hafner, J. Ab Initio Molecular Dynamics for Liquid Metals. *Phys. Rev. B* **1993**, *47* (1), 558–561.
- (40) Grimme, S.; Antony, J.; Ehrlich, S.; Krieg, H. A Consistent and Accurate Ab Initio Parametrization of Density Functional Dispersion Correction (DFT-D) for the 94 Elements H-Pu. *J. Chem. Phys.* **2010**, 132 (15), 154104.
- (41) Gunda, H.; Das, S. K.; Jasuja, K. Simple, Green, and High-Yield Production of Boron-Based Nanostructures with Diverse Morphologies by Dissolution and Recrystallization of Layered Magnesium Diboride Crystals in Water. *ChemPhysChem* **2018**, *19* (7), 880–891.
- (42) James, A. L.; Jasuja, K. Chelation Assisted Exfoliation of Layered Borides towards Synthesizing Boron Based Nanosheets. *RSC Adv.* **2017**, *7* (4), 1905–1914.
- (43) Radisavljevic, B.; Radenovic, A.; Brivio, J.; Giacometti, V.; Kis, A. Single-Layer MoS2 Transistors. *Nat. Nanotechnol* **2011**, *6* (3), 147–150.
- (44) Das, S. K.; Bedar, A.; Kannan, A.; Jasuja, K. Aqueous Dispersions of Few-Layer-Thick Chemically Modified Magnesium Diboride Nanosheets by Ultrasonication Assisted Exfoliation. *Sci. Rep* **2015**, *5* (1), 1–11.
- (45) Holder, C. F.; Schaak, R. E. Tutorial on Powder X-Ray Diffraction for Characterizing Nanoscale Materials. *ACS Nano* **2019**, 13, 7359–7365.
- (46) Wang, Y.; Zhang, M.; Kang, Z.; Shi, L.; Shen, Y.; Tian, B.; Zou, Y.; Chen, H.; Zou, X. Nano-Metal Diborides-Supported Anode Catalyst with Strongly Coupled TaOx/IrO2 Catalytic Layer for Low-Iridium-Loading Proton Exchange Membrane Electrolyzer. *Nat. Commun.* 2023, 14 (1), 5119.
- (47) Zhu, H.; Hu, J.; Zhang, Z.; Zhuang, Z.; Hao, J.; Duan, F.; Lu, S.; Wang, X.; Du, M. Lewis Acid Sites Incorporation Promotes CO2 Electroreduction to Multicarbon Oxygenates over B-CuO Nanotubes. *Appl. Catal., B* **2023**, 339, No. 123082.
- (48) Liu, M.; Rao, F.; Balamurugan, J.; Liang, T.; Liu, C. Theoretical Research on Efficient Electrocatalysis of CO2 Reduction Reaction by Borophene Loaded Transition Metals. *Surfaces and Interfaces* **2024**, 49, No. 104454.
- (49) Mir, S. H.; Yadav, V. K.; Singh, J. K. Efficient CO₂ Capture and Activation on Novel Two-Dimensional Transition Metal Borides. *ACS Appl. Mater. Interfaces* **2022**, *14* (26), 29703–29710.
- (50) Morales, D. M.; Risch, M. Seven Steps to Reliable Cyclic Voltammetry Measurements for the Determination of Double Layer Capacitance. *Journal of Physics: Energy* **2021**, *3* (3), No. 034013.
- (51) Connor, P.; Schuch, J.; Kaiser, B.; Jaegermann, W. The Determination of Electrochemical Active Surface Area and Specific Capacity Revisited for the System MnO x as an Oxygen Evolution Catalyst. Zeitschrift für Physikalische Chemie 2020, 234 (5), 979–994.
- (52) Liu, W.; Zhai, P.; Li, A.; Wei, B.; Si, K.; Wei, Y.; Wang, X.; Zhu, G.; Chen, Q.; Gu, X.; Zhang, R.; Zhou, W.; Gong, Y. Electrochemical CO2 Reduction to Ethylene by Ultrathin CuO Nanoplate Arrays. *Nat. Commun.* **2022**, *13*, 1877.
- (53) Zhang, W.; Huang, C.; Xiao, Q.; Yu, L.; Shuai, L.; An, P.; Zhang, J.; Qiu, M.; Ren, Z.; Yu, Y. Atypical Oxygen-Bearing Copper Boosts Ethylene Selectivity toward Electrocatalytic CO ₂ Reduction. *J. Am. Chem. Soc.* **2020**, *142* (26), 11417–11427.
- (54) Sheldon, R. A. Metrics of Green Chemistry and Sustainability: Past, Present, and Future. *ACS Sustain Chem. Eng.* **2018**, 6 (1), 32–48.
- (55) Grammatico, D.; Bagnall, A. J.; Riccardi, L.; Fontecave, M.; Su, B.; Billon, L. Heterogenised Molecular Catalysts for Sustainable Electrochemical CO ₂ Reduction. *Angew. Chem., Int. Ed.* **2022**, *61* (38), No. e202206399.
- (56) Grim, R. G.; Huang, Z.; Guarnieri, M. T.; Ferrell, J. R.; Tao, L.; Schaidle, J. A. Transforming the Carbon Economy: Challenges and Opportunities in the Convergence of Low-Cost Electricity and Reductive CO ₂ Utilization. *Energy Environ. Sci.* **2020**, *13* (2), 472–494.
- (57) Han, G. H.; Bang, J.; Park, G.; Choe, S.; Jang, Y. J.; Jang, H. W.; Kim, S. Y.; Ahn, S. H. Recent Advances in Electrochemical,

- Photochemical, and Photoelectrochemical Reduction of CO ₂ to C ₂₊ Products. *Small* **2023**, *19* (16), No. 2205765.
- (58) Liu, J.; Guo, C.; Vasileff, A.; Qiao, S. Nanostructured 2D Materials: Prospective Catalysts for Electrochemical CO₂ Reduction. *Small Methods* **2017**, *1*, No. 1600006.
- (59) Liu, H.; Zhu, Y.; Ma, J.; Zhang, Z.; Hu, W. Recent Advances in Atomic-Level Engineering of Nanostructured Catalysts for Electrochemical CO ₂ Reduction. *Adv. Funct. Mater.* **2020**, 30 (17), No. 1910534.